Frequency-Domain Active Contours Solution to Evaluate Intima-Media Thickness of the Common Carotid Artery

M.C. Bastida-Jumilla, R.M. Menchón-Lara, J. Morales-Sánchez, R. Verdú-Monedero, J. Larrey-Ruiz, J.L. Sancho-Gómez

Departamento de Tecnologías de la Información y las Comunicaciones
Universidad Politécnica de Cartagena

Abstract

The intima-media thickness (IMT) of the common carotid artery (CCA) is being used as a reliable and early detector of atherosclerosis. Atherosclerosis may be unnoticed fo years before triggering severe illnesses such as stroke, embolisms or ischemia. Hence, the use of IMT leads to an early atherosclerosis diagnosis that can prevent more serious cardiovascular diseases. Usually, IMT is manually extracted from ultrasound images, which is a non-invasive technique, but unfortunately its measurement is prone to error.

This paper addresses a fully automatic method to segment the artery layers of the CCA over ultrasound images. Unlike other methods, the segmentation is not restricted to IMT, the artery diameter can be extracted too, which can help to determine cardiovascular risk together with IMT. The proposed technique is based on a frequency-domain implementation of active contours, which are computationally faster than the original space-formulation, while providing soft final contours.

Working with three different probes over a range of spatial resolutions from 0.029 mm/pixel to 0.081 mm/pixel, the method presents an IMT error of only 13.8 ± 31.9 μm (in mean ± standard deviation) when tested on an database containing 46 images. The automatic results were compared to the

Email addresses: consuelo.bastida@upct.es (M.C. Bastida-Jumilla), rmml@alu.upct.es (R.M. Menchón-Lara), juan.morales@.upct.es (J. Morales-Sánchez), rafael.verdu@upct.es (R. Verdú-Monedero), jorge.larrey@upct.es (J. Larrey-Ruiz), josel.sancho@upct.es (J.L. Sancho-Gómez)

average of 2 manual observations performed by 2 observers (4 observations) over each image in our database.

Keywords: image segmentation, active contours, ultrasound images, intima-media thickness

---

1. Introduction

Cardiovascular diseases (CVD) are one of the main causes of death in developed countries [1]. Therefore, it is of paramount importance to prevent and to monitor patients affected by a CVD. Atherosclerosis is a CVD that acts as a trigger for more serious conditions, such as stroke, embolism or ischemia. Thus, an early diagnosis is critical to prevent related pathologies. Atherosclerosis consists of a progressive thickening of the arterial walls by fat accumulation, which hinders blood flow and reduces the elasticity of the affected vessels.

The intima-media thickness (IMT) of the common carotid artery (CCA) is one of the mostly used indicators of cardiovascular risk [2, 3, 4]. IMT is extracted from ultrasound images [5] (i.e., a non-invasive technique) and can diagnose atherosclerosis in its early stages, when the patient is still asymptomatic.

By measuring and monitoring the IMT variations doctors are able to early detect small thickening of the artery walls and, thus, to prescribe preventive care. Several manual measurement procedures appear in medical bibliography [3, 2, 6], but in order to consider IMT as a reliable indicator of atherosclerosis, the measurement protocol must prove its repeatability and reproducibility [2, 7]. Particularly, the method here proposed is based on the repeatable and reproducible protocol used by the Radiology Department from Hospital Universitario Virgen de la Arrixaca [7], which provided the images to develop our method.

As can be seen in Figure 1 (left), blood vessels present three different layers, from innermost to outermost, intima, media and adventitia. These layers can be seen in a longitudinal cut of the CCA over the near and the far wall (Fig. 1 (right)). In the middle, the channel where blood flows known as lumen is appreciated as a dark area corresponding to a liquid medium. The IMT is defined as the distance from the lumen-intima to the media-adventitia interface at far wall. The interfaces to be detected present a bright-dark-bright pattern corresponding to the intima-media-adventitia layers (see Fig. 1).

In the manual procedure [7] an expert observer marks from one to three pair of points delimiting IMT around 1 cm after the carotid bulb. The carotid bulb is located on the left of the image in all cases.

This paper addresses a fully automatic method to segment lumen-intima (LI) and media-adventitia (MA) interfaces along with the near wall-lumen

interface. IMT measurement is the main objective and more precise, but the lumen diameter (LD) is provided too. Therefore, with little extra computational cost the method provides complementary information apart from the IMT.

Unlike manual procedure, with the proposed method it is posiible to measure IMT along a certain artery length and to calculate statistics of IMT and CCA diameter, such as mean, median or maximum. Since the proposed method applies automatic image processing, the results are reproducible, subjectivity is avoided and the analysis of IMT over a large population can be optimized in terms of time.

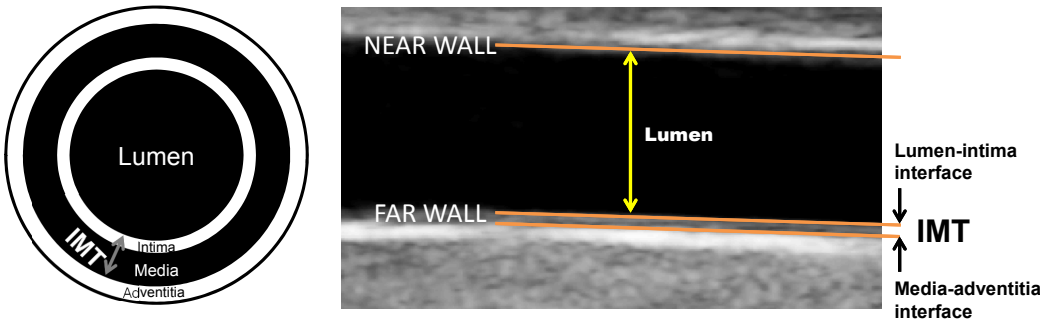

Figure 1: Blood vessel layers in a transverse (left) and longitudinal section (right) of the vessel.

This work is structured as follows; the present section introduces the need of automated techniques to measure IMT of the CCA from ultrasound images and describe the image database used. In the Materials and Methods section (2), the image database and features of manual observations are provided, together with the presentation of the developed method. Results are presented in Section 3 and discussed in Section 4. Finally, the conclusion section closes the paper.

2. Materials and Methods

2.1. Materials

2.1.1. Image database

Our image database consists of 46 ultrasound images of a longitudinal cut of the CCA taken with a Philips iU22 Ultrasound System at different scale resolutions (ranging from 0.029 mm/pixel to 0.081 mm/pixel). Three

different probes have been used at the discretion of the specialist, with frequency ranges of 9-3 MHz, 12-5 MHz and 17-5 MHz. The radiologist could manually select the space resolution of the image and the parameters of the US machine. The images correspond to 27 patients aged from 25 to 71, 12 of them females. The average age was 56.

For the sake of homogeneity, the images were taken following certain recommendations: CCA preferably horizontal, the carotid bulb should not appear, CCA should be located approximately in the middle of the image and without blood turbulences. However, some images in our database do not obey these guidelines. There are 12 with blood turbulences, 16 sloped CCA, 1 elongated CCA, 6 noisy images and 19 images in which the bulb appears. Since the carotid bulb is curved, the typical bright-dark-bright pattern is not always present and active contours may diverge near the bulb.

The inclusion of these images, apparently inconvenient for our purposes, is used to assess the robustness of the developed method, which demands less strict requirements in future US image acquisitions.

2.1.2. Ground truth contours

The automatic delineation is compared to 4 manual segmentations from 2 different observers. Each observer made two measurements of every image spaced at least one month, which implies 184 observations. Thus, each of the 46 manual results were calculated as the average contours of 4 different observations.

Hereafter, for every single image, these observations will be referred to as:

- MA1: first measurement from observer A.
- MA2: second measurement from observer A.
- MB1: first measurement from observer B.
- MB2: second measurement from observer B.

The delineation was performed over the images manually by marking at least 10 points for each contour. The manual contours were acquired thanks to a Matlab software implemented by the authors. After manual drawing, the selected points were lineally connected and saved. Therefore, for a single image, there are 4 manual contours for each of the 3 interfaces to be detected. As ground truth contours for a single image, the mean of these 4 manual delineations is considered.

2.1.3. IMT metrics

IMT distance is calculated using Mean Absolute Distance (MAD), Polyline Distance (PD) [8], Center Line Distance (CLD) [9] and Haussdorf Distance (HD) [10]. These metrics are used for another purpose too, the comparison of the manual and automatic contours.

2.2. Methodology

A fully automatic method is presented. The method first makes a rough segmentation of the lumen followed by a fine segmentation of the CCA walls by means of a frequency-based implementation of active contours. User interaction is not required; it extracts the carotid diameter together with the IMT and provides satisfactory results with different ultrasound image resolutions.

The proposed method to segment the CCA layers comprises three steps (see Fig. 2). First of all, the lumen is delimited to calculate initial contours. After that, the CCA layers are segmented via active contours implemented in the Fourier domain and using B-splines as shape function. Finally, an automatic checking of the contours is performed. This checking step is previous to the analysis of the results by medical staff.

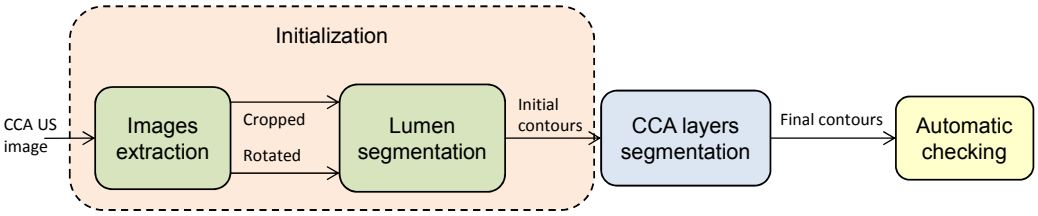

Figure 2: Flow chart of the method.

2.2.1. Initialization

As can be seen in Fig. 2, two inputs are required to detect the far wall, a crop of the raw image containing only the CCA and the original image rotated so that the CCA is horizontally oriented. From these images, lumen is segmented to extract the initial contours for the active contours algorithm.

Images extraction

- Image crop
  CCA longitudinal cut in ultrasound images includes not only the CCA itself, but also patient data, resolution, date and other unnecessary data

to segment the CCA layers superimposed over the US image. Thus, the original image is cropped (see Fig. 3 left). Morphological closing and opening using a horizontal structuring element (1×5 pixels) is applied over the gradient image. Outer columns and rows of the resulting image are removed if the sum of the corresponding column or row is zero. This automatical crop of the image is useful when there is no access to the DICOM fields that provide the limits of the ultrasound region or when they are empty.

- Image rotation
  In the lumen segmentation step, a correlation of the image with a horizontal model of the far-wall pattern is performed. To improve the performance of the correlation, the artery orientation is corrected to make it horizontal too.

  A Sobel directional filtering is applied over the original cropped image. As a result, the horizontal edges of the image are obtained. Then, over the edges, a Hough transform [11] is performed to detect the main 5 directions in the image. The longest line found via the Hough transform is selected as the main direction of the artery. Finally, a bilinear interpolation rotates the image. The whole process is depicted in Fig. 3, where, from left to right, we can see a raw image, its crop, the Sobel edges of the crop with the Hough lines superimposed and the rotated image.

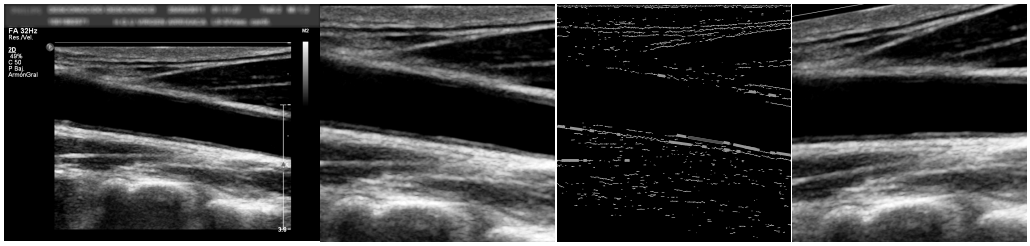

Figure 3: From left to right: Raw image, cropped image, edges of the cropped image with the Hough lines overimposed and rotated image.

Lumen segmentation

The different steps to segment the lumen automatically comprises:

1. Far wall detection
   The rotated image is correlated with a softened crop of an actual ultra-

sound image containing the intima-media-adventitia pattern (see Fig. 4). The maximum of correlation indicates the vertical location of the far wall in the image.

2. Iterative median filtering
   With this filtering, speckle noise is reduced while the lumen boundaries are preserved [12] and the different regions of the image become smooth and homogeneous. The filter is horizontally oriented, with size 5×15 pixels and applied 10 times to attenuate backscattering and speckle noise in the lumen area.
3. Otsu's binarization and negative of the image
   The output of this step consists of a binary image with isolated white regions.
4. Selection of the lumen region
   Amongst the different regions obtained in step 3, the one corresponding to the lumen must include the maximum of correlation calculated in step 1 (see Fig. 4).

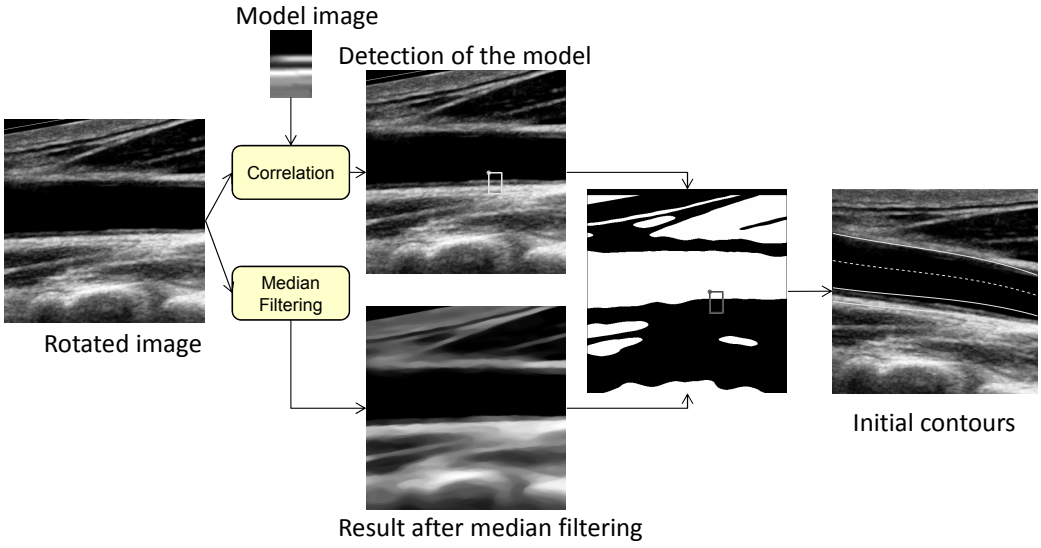

Figure 4: Lumen segmentation process (left) and initial contours (right).

Then, lumen boundaries are interpolated with an order 3 polynomial to smooth the contours. A near-far wall border is calculated as the mean vertical position between the upper and lower edge of the lumen. This border will

be used in the following sections (shown as dashed line in the right image in Fig. 4).

Finally, to assure a height range that includes the borders to be detected, near wall boundary is displaced 0.3 mm downwards, while far wall edge is displaced 0.8 mm upwards and duplicated 1.65 mm (more than 3 times a healthy IMT) downwards from the latter (see right image in Fig. 4). These displacement values have been obtained by experimental adjustment.

2.2.2. Active Contours CCA layers segmentation

Frequency implementation of Active Contours

Active contours or snakes [13] are based on physical models of elastic bodies. Therefore, its evolution in time and space is determined by internal forces (i.e., inner characteristic such as elasticity or rigidity) and external forces, which deform and attract the contours.

The discrete implementation of the active contours entails the calculation of the inverse of a $N \times N$ matrix (having each contour N nodes), which requires a high computational cost. To reduce it, the proposal by Weruaga et al. [14] of using a frequency formulation is implemented. The computational savings vary from N^2 in the classical formulation to $Nlog_2N$, being N the number of nodes.

Conventionally, to construct the contour, each of the N nodes in contour $\mathbf{u}$ is assembled with N piecewise polynomials, , obtaining additional points in the contour called control points v. In our case, cubic B-spline is the shape function used. Cubic B-splines are robust to noise and present good performance-running time ratio [15].

The segmentation of the CCA layers reduces to an iterative evolution of the initial contours, as can be seen in Fig. 5. To achieve rigid behaviour, the elasticity and rigidity parameters have been fixed to $\alpha = 0$ and $\beta = 1$, respectively.

External forces are combined with gravity and take-off forces. The calculation of the external, take-off and gravity forces is detailed below.

The position of the nodes in the next iteration is calculated always keeping in mind that no contour must cross another one nor cross the near-far wall border calculated in section 2.2.1. If the combined displacement of the far wall contours is less than 0.02% of the vertical size of the image, their evolutions stop, while if the near wall contour presents a displacement less than 0.085% of the vertical dimension, it stops too. These stop conditions

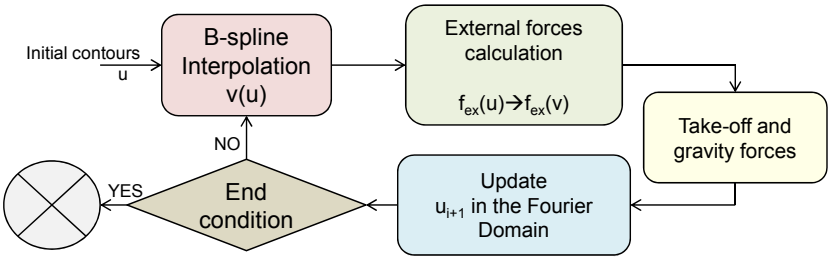

Figure 5: Flow chart of the active contours algorithm implementation.

were empirically optimized in order to detect when the active contours have converged.

External forces calculation

After initializing the contours, the external forces are calculated (see Fig. 6). First of all, a softening of the image consisting of a low pass filter is applied. At this point, the artery shows a quasi-horizontal orientation, thus the intensity changes of the artery layers take place mainly in the vertical direction. Therefore, to reduce computational cost, the gradient will be computed only in the vertical axis.

Nevertheless, the intensity transition in the near wall-lumen interface is from bright to dark (negative gradient) and for the far wall is from dark to bright (positive gradient). Both kind of transitions are combined in a single image by using the border b calculated in 2.2.1 (see Fig. 7). This border stablishes the borderline between near b_{nw} and far wall b_{fw} regions. Being $\hat{I}$ the softened cropped image, $g\{\cdot\}$ the vertical gradient operator and $s = (x, y)$ the position of a pixel in $\hat{I}$, the combined gradient image $g_c(\hat{I})$ can be described as

$$g_c(I\hat{(}s)) = \begin{cases} abs(g(\hat{I}))|g(\hat{I}) < 0) & if \quad s \in b_{nw} \\ g(\hat{I})|g(\hat{I}) > 0 & if \quad s \in b_{fw} \end{cases} \tag{1}$$

To eliminate more undesired structures, a morphological reconstruction [16] is performed using a morphological mask containing only a selection of elements of the image oriented in the main directions of the artery. Before the reconstruction, a soft morphological processing is performed to remove small structures, achieving a gradient image with reduced noise.

In order to perform the reconstruction, we use a morphological mask as marker containig the main directions of the noise reduced gradient image.

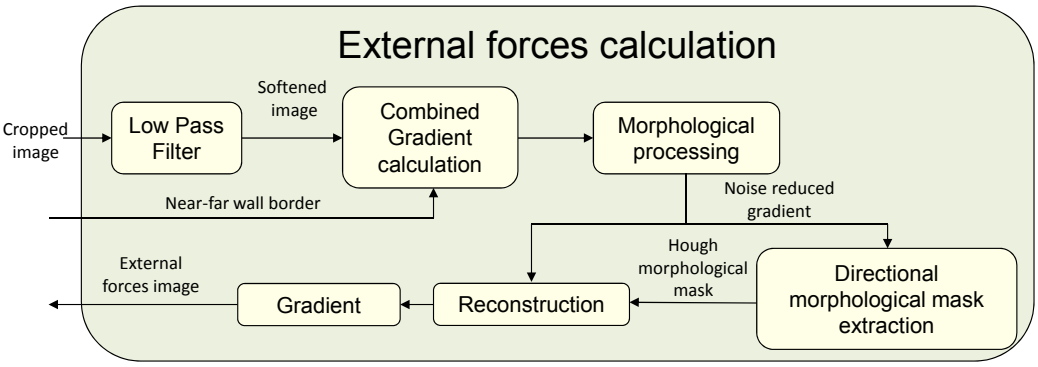

Figure 6: External forces calculation.

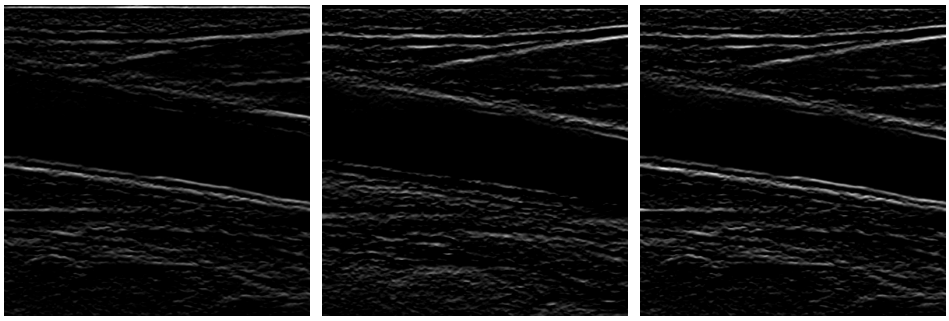

Figure 7: Positive (left), negative (centre) and combined gradient transitions (right).

Fig. 8 shows a diagram with the mask calculation process. After downsampling by a factor 2, Canny edges of the image are computed. By applying a Hough transform over these edges, the 3 main directions in the image are extracted (Fig. 9, left). Then, several openings are performed over the gradient image with reduced noise, using the lines provided by the Hough transform as structuring elements. The accumulation of the openings is used as the marker image in the reconstruction process (Fig. 9, centre). After the reconstruction the resulting image is clearer and less noisy (Fig. 9, right).

Finally, from the reconstructed image g_r, external forces F_{ext} are computed as

$$F_{ext} = \nabla |g_r| + c \tag{2}$$

being c a constant from the gravity and take-off forces. These forces act in case the contour is not attracted by any edge during the first iterations. Gravity forces drive lumen-intima contour downward, whereas take-off forces

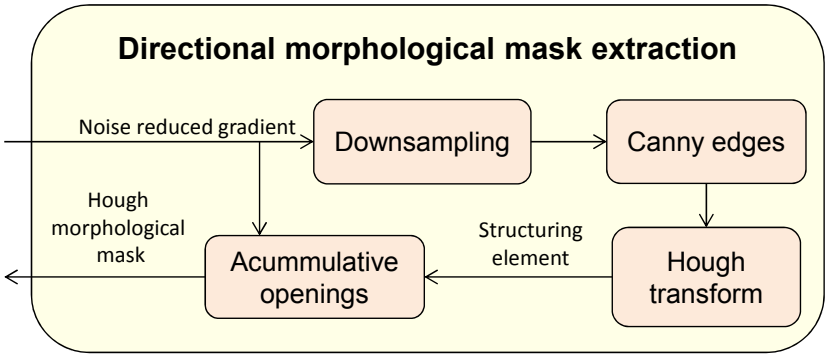

Figure 8: Morphological mask extraction.

Figure 9: Mask (left), marker (centre) and reconstructed (right) images.

drive near wall-lumen and media-adventitia contours upwards

The segmentation after the active contour algorithm is shown in Fig. 10.

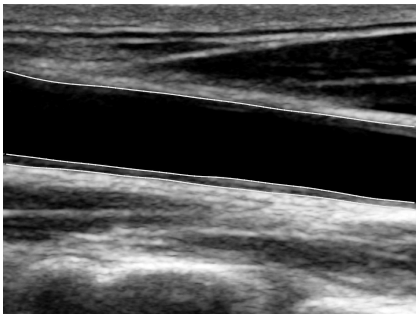

Figure 10: Segmentation after active contour algorithm.

2.2.3. Automatic checking of the contours

This step avoids considering measurements in case the snakes do not converge to the valid solution, e.g. in areas where there is no bright-dark-bright intensity pattern (see Fig. 11 centre, where solid lines correspond to checked sections and dashed lines represent unchecked sections). On the left of the image (Fig. 11 centre), the active contours algorithm has not reached the correct edge, mainly because there the far wall pattern is imperceptible.

To check and refine the curves, we focus on finding a bimodal vertical profile of the far wall in the gradient image, i.e. one peak for the lumen-intima interface and another for the media-adventitia interface. The search of this bimodal intensity profile in the gradient image is made by combining two strategies:

- Statistical strategy
  As can be expected from bimodal intensity profiles, the set of vertical distances between lumen-intima and media-adventitia segmented interfaces results into a dataset with pseudo-normal distribution (see Fig. 11 left). The obtained dataset contains the IMT estimations, and can present outliers in case of inadequate layer segmentation, as is the case in Fig. 11 centre (see dashed segments of the contours). Since a healthy adult CCA presents an IMT from 0.5 mm, all the measurements under 0.4 mm are discarded. Then, the IMT distribution is multiplied by a Gaussian window and thresholded to eliminate outliers. In Fig. 11 left, over the IMT histogram the Gaussian window is drawn and the discarded values of distance are represented in white bars. The centre of the window is placed on the median of the IMT distribution and the standard deviation of the Gaussian window is the spatial resolution of the image.

- Intensity-based strategy
  The second strategy consists of finding a dark region surrounded by gradient intensity peaks, located over the segmented layers. Intensity peaks are found via a 2-means classification (peaks and gaps classes) from the intensity values of the reconstructed gradient image. Next, successively for each corresponding pair of control points, one in the MA contour and other in the LI contour, a vertically-oriented profile is extracted from the gradient image. The gradient profile ranges from one control point location to anther one, comprising them. A pair of

control points is marked as valid if the respective profile encloses a gap between two intensity peaks.

Finally, the automatic checking stage consists of:

1. Combination of strategies
   The goal is to distinguish between valid and non-valid segments by combining both strategies (statistical and intensity-based) with an AND operator.
2. Node validation and repositioning
   A polynomial adjustment is applied over non-valid sections surrounded by long validated sections (20 control points). The nodes are relocated only in the non-valid sections to check if they accomplish the intensity-based strategy in their new positions.
3. Intensity-based strategy with gamma correction
   Finally, a second intensity-based checking, like in step 1, is performed with the new node positions. The 2-means classification is performed over a gamma correction ($\gamma = 2$) of the reconstructed gradient image to enhance edges. This last checking step affects only to those sections previously classified as non-valid, which results in longer valid sections.

The final result for the example image can be seen in Fig. 11 right.

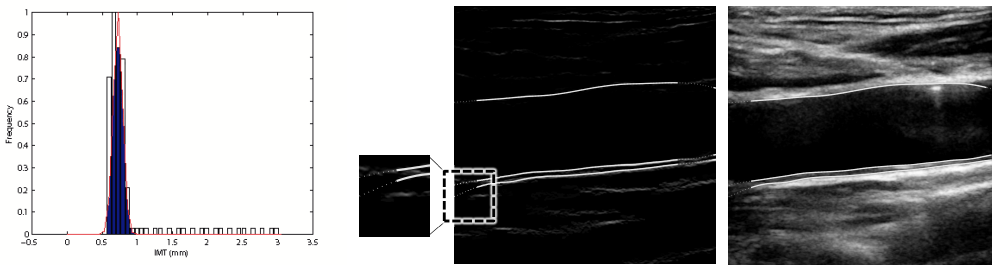

Figure 11: Statistical checking process: (left) IMT histogram, (centre) segmentation over the gradient image and final segmentation (right).

3. Results

3.1. Manual measurements

As can be inferred from Table 1, the IMT intraobserver reproducibility is of 98.73% for observer A and of 98.27% for observer B. The IMT measurement

Table 1: Correlation of the 4 IMT manual measurements (MAD)

		ρ	Mean difference ± standard deviation (μm)
IMT	MA1 vs MB1	97.14%	4.4 ± 50.9
	MA1 vs MB2	96.59%	3.7 ± 56.6
	MA2 vs MB1	97.36%	10.3 ± 47.9
	MA2 vs MB2	97.32%	9.6 ± 50.3
	MA1 vs MA2	98.73%	5.9 ± 34.1
	MB1 vs MB2	98.27%	0.67 ± 41.6
LD	MA1 vs MB1	97.17%	5.1 ± 50.8
	MA1 vs MB2	96.62%	4 ± 56.3
	MA2 vs MB1	97.24%	11.8 ± 48.8
	MA2 vs MB2	97.33%	10.7 ± 50.1
	MA1 vs MA2	98.74%	-6.7 ± 34
	MB1 vs MB2	98.21%	-1.1 ± 42.2

difference presents a value in mean ± standard deviation of 5.9 ± 34.1 μm for observer A and 0.67 ± 41.6 μm for observer B when IMT is measured as the Mean Absolute Distance (MAD) between the LI and MA interfaces.

For the LD, the intraobserver reproducibility is of 98.74% for observer A and 98.21% for observer B.

The interobserver reproducibility for the IMT shows a correlation coefficient betweeen 96.62% and 97.33%.

Since the manual measurements present good repeatability and reproducibility, the average contours are considered as ground truth. Thus, the automatic contours are compared to the mean of MA1, MA2, MB1 and MB2 contours.

Similar distributions of the IMT (measured as MAD) are obtained for the 4 manual observations, as can be seen in Table 2.

3.2. Visual results

In Fig. 12 some IMT segmentation results are shown for different cases: (a) a good quality image, (b) an image with gaps in the interfaces to be detected, (c) an image in which the carotid bulb is noticeable, (d) a noisy image and (e) a sloping CCA image, respectively. For all of them, final

Table 2: MAD IMT statistics for the manual measurements

Observation (mm)	Q1	Median	Q3	Mean ± std
MA1	0.48681	0.60275	0.79144	0.6690 ± 0.2142
MA2	0.50621	0.60637	0.80653	0.6749 ± 0.2097
MB1	0.49895	0.59294	0.78624	0.6646 ± 0.2049
MB2	0.48966	0.60206	0.74559	0.6652 ± 0.2182

checked contours are shown in solid line, whereas unchecked sections are drawn in dashed line. Notice that the better image quality, the longer valid sections are. In all cases, a good segmentation of the CCA layers is achieved and the automatic checking step avoids the inclusion of wrong sections in IMT segmentation, and, consequently, in the IMT statistics. These wrong sections occur mainly under two scenarios, when there is no intensity in the LI interface and when the CCA presents some curvature (because it is an elongated CCA or the bulb is visible).

Manual and automatic IMT and LD statistics of the images in Fig. 12 when measured as MAD are shown in Table 3.

In Fig. 13 enlarged regions of the corresponding images in Fig. 12 are shown. Automatic contours are drawn in solid line, whereas manual ground truth contours are drawn as dashed lines.

Table 3: Segmentation results (measurements are given in mean ± standard deviation in mm)

Image	$\mathbf{IMT_{auto}}$	$\mathbf{IMT_{manual}}$	$\mathbf{LD_{auto}}$	$\mathbf{LD_{manual}}$
Fig. 12(a)	0.46 ± 0.032	0.44± 0.028	5.85 ± 0.31	5.95 ± 0.22
Fig. 12(b)	0.77 ± 0.041	0.78± 0.085	8.35 ± 0.55	8.38 ± 0.52
Fig. 12(c)	0.59 ± 0.069	0.58 ± 0.046	5.57 ± 0.25	5.99 ± 0.62
Fig. 12(d)	0.83 ± 0.2	0.89 ± 0.14	7.27 ± 0.19	7.22 ± 0.18
Fig. 12(e)	0.66 ± 0.062	0.69 ± 0.072	6.53 ± 0.37	6.45 ± 0.15

3.3. Automatic measurements and statistics

Starting from automatic final contours, the previously introduced metrics (see section 2.1.3) are used for two purposes: compare ground truth contours

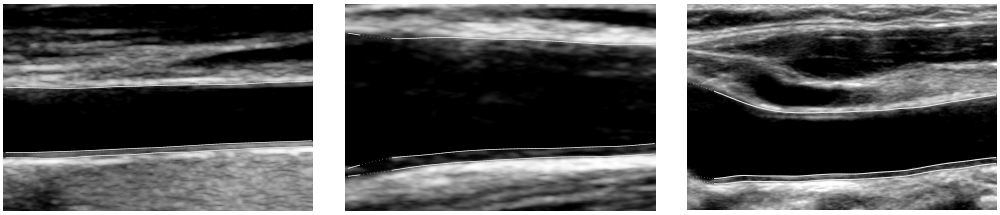

(a) Result for a good quality image

(b) Result with gaps in the IMT interfaces.

(c) Result for an image with bulb.

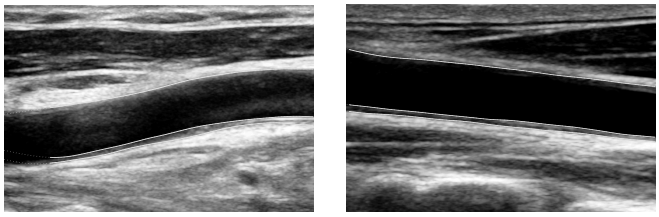

(d) Result for noisy image.

(e) Result for a sloping CCA.

Figure 12: Segmentation results

with the automatic segmentation and measure the IMT and the LD. Thus, the similarity of single manual and automatic contours and the final IMT and LD measurement (manual and automatic) are compared, all measurements computed with four different metrics.

- Manual vs. automatic IMT measurements
  In Fig. 14 the Bland-Altman's plot [17] of the manual vs. automatic mean IMT results for MAD, PD, CLD and HD, respectively, are shown. The vertical axis in the Bland-Altman's plots represents manual minus automatic measurement. Horizontal axis in the Bland-Altman's plot represents the average of the manual and automatic observation.

  Pearson correlation coefficient ρ, error variance $var(e)$ and mean IMT and LD error (in mean $\pm$ standard deviation) can be seen in Table 4.

  In Fig. 15, the boxplot distributions of the manual and automatic IMT measurement are shown. Upper and lower box limits represent $Q3$ and $Q1$, respectively. The middle red line lies over the median of the distribution ($Q2$). Maxima and minima are represented as upper and lower whiskers. The measurements considered as outliers (within a confidence interval of 97.5%) are marked as crosses.

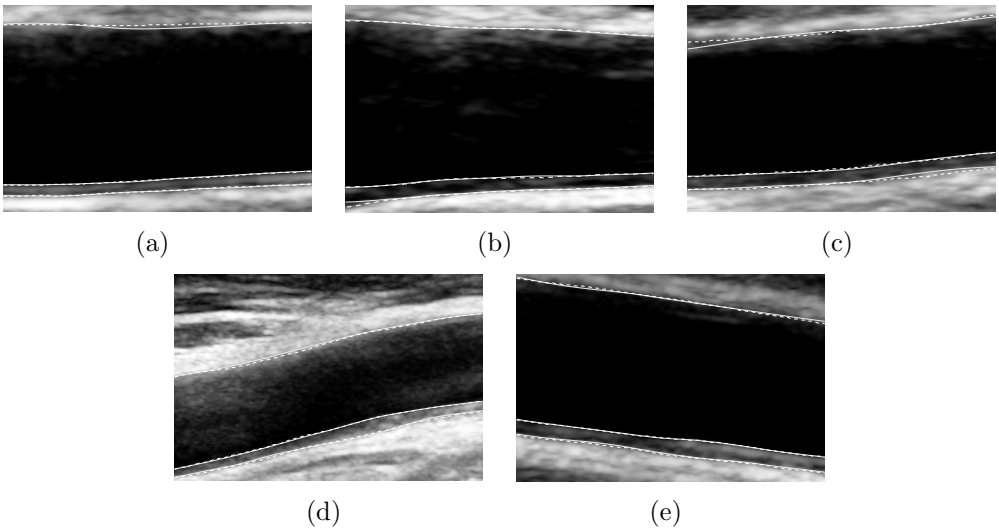

Figure 13: Automatic (solid lines) vs. manual (dashed lines) delineation over enlarged areas of the images in Fig. 12

- Manual vs. automatic LD measurements
  In Fig. 16 the Bland-Altman plot of the LD measured as MAD is shown together with its boxplot.

- Distances between manual and automatic contours
  In Table 5, the mean distance ± standard deviation between manual and automatic contours is displayed for the considered metrics.

4. Discussion

The described method has achieved the NWI, LII and MAI segmentation by means of a frequency implementation of the active contours algorithm. Thus, it provides automatically the IMT and LD measurements from a longitudinal CCA ultrasound image. The results were compared to ground truth contours, which were calculated as the average of 4 manual delineations for each image. In the following subsections a brief review of related method can be found. After that, the results obtained by the presented method are discussed and compared to already existing methods.

Table 4: Correlation coefficient, error variance (mm^2) and error (mean difference ± std in µm) of the IMT for MAD, PD, CLD and HD of the manual vs. automatic IMT measurement

	metric	ρ	$var(e)(mm^2)$	$e \pm std(\mu m)$
IMT	MAD	0.9901	0.001	13.8 ± 31.9
	PD	0.9901	$9.4 \cdot 10^{-4}$	10.1± 30.7
	CLD	0.9898	$9.3 \cdot 10^{-4}$	8.3 ± 30.5
	HD	0.9471	0.0066	-4.8 ± 81.2
LD	MAD	0.9922	0.0217	-65.4 ± 147.4
	PD	0.9923	0.0215	-54.3 ± 146.5
	CLD	0.9911	0.0247	-53.0 ± 157
	HD	0.9420	0.1850	54.9 ± 430.2

Table 5: Distances between manual and automatic contours (in mm) for the metrics considered (mean ± standard deviation

Metric	LII	MAI	NWI
MAD	0.0330 ± 0.0152	0.0424 ± 0.0185	0.1098 ± 0.1082
PD	0.0347 ± 0.0154	0.0440 ± 0.0182	0.1133 ± 0.1062
CLD	0.0315 ± 0.0141	0.0413 ± 0.0187	0.1086 ± 0.1074
HD	0.5772 ± 0.8330	0.5873 ± 0.8315	0.8426 ± 1.3131

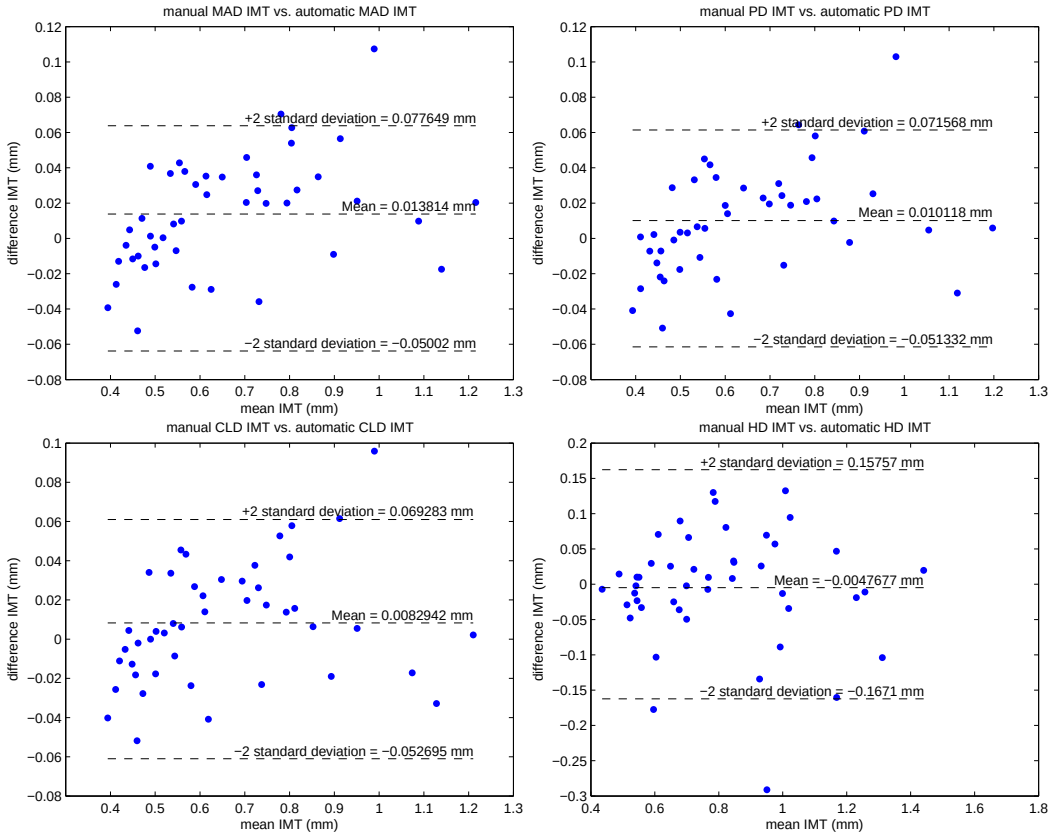

Figure 14: Bland-Altman plots for IMT (manual vs. automatic measurement) for MAD, PD, CL and HD metrics

4.1. Background

Since IMT has been used as an early and reliable indicator of cardiovascular risk, several methods have appeared to provide more accurate IMT measurements. The first attempts correspond to Gustavsson et al. [18, 19, 20]. The main idea is to analyze the gradient of the image in vertical cuts to determine the positions of the interfaces to be detected. Then, dynamic programming is used to optimize a cost function to establish the positions of the lumen-intima and media-adventitia interfaces. Despite the inclusion of a continuity term, the data are still locally-derived. Besides, all of these methods require some user interaction to select the region of interest.

Other authors propose active contours to segment the carotid layers [21, 22, 23] or a combination with other techniques, like dynamic programming

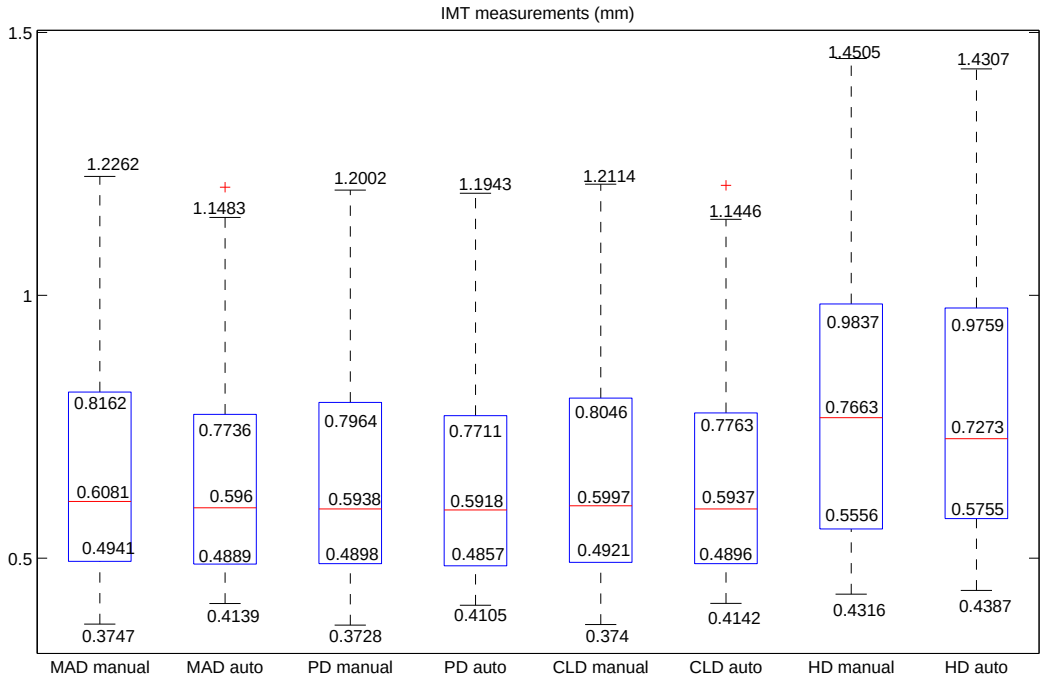

Figure 15: Boxplot of IMT for manual and automatic contours.

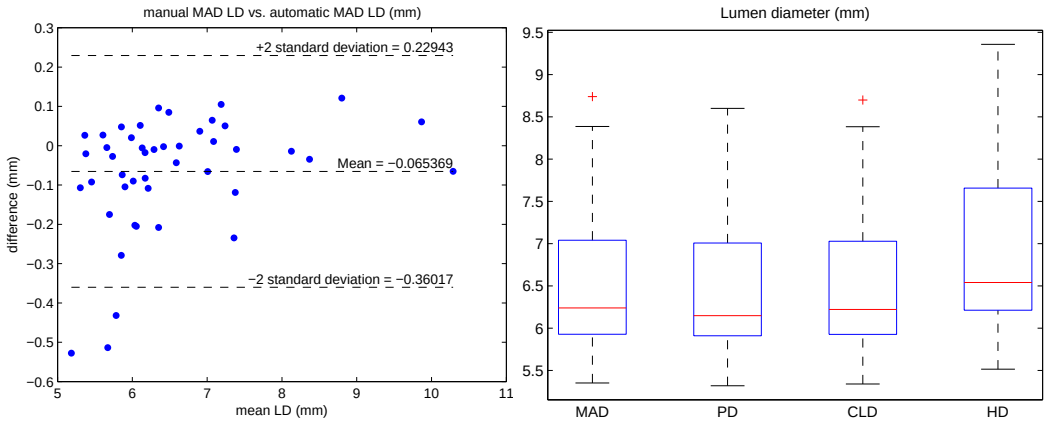

Figure 16: Bland-Altman plot and boxplot for MAD LD

[24]. However, since initialization is crucial in active contours performance, most of them still required manual initialization of the contours. The use of active contours provides a solution based on global information of the US image, giving thus, softer final contours than methods based on locally-

derived data.

There exists other approaches based on Nakagami distribution [25], Hough transform [26, 27] or RANSAC algorithm [28], but they still lack automation.

According to the degree of automation, all the techniques in the literature can be clasified as user-independent or user-dependent [29]. User-independent or fully automatic techniques do not require any user interaction and present better time performance since they are usually designed to process several images in a short period of time. However, to make the full automation possible they need a common framework, that is, images without plaques, carotid horizontally oriented, images with fixed resolution, etc. Unlike the former techniques, user-dependent or semi-automated techniques are more flexible with respect to the initial conditions and present more accurate results. This is due to the manual selection of the region of interest. An expert observer can easily extract the portion of the image were the IMT measurement is optimum, thus, helping the segmentation algorithm.

To the authors' knowledge, it is not until Delsanto's proposal [30] that a fully automatic method can be found. The same group of authors have presented different fully automatic methods, which present good performance in the absence of blood turbulences. Even though some of them admit the presence of plaques, they work with images presenting the same resolution [31, 32, 33, 34, 35]. These proposals implement two stages, one to initialize the contours and a second one to segment the artery walls. Following the same idea, other authors have proposed methods based on models [36] or different implementations of active contours [37, 38], like active contours without edges [39] based on the Chan-Vese snake [40], or frequency-formulation of active contours [41]. The latter, needs to perform twice the active contour segmentation ,increasing the computational cost, and this work lacks the comparison of the results with a ground truth segmentation. Other works are based on the use of FOAM [42] or neural networks [43].

Most of the former methods do not segment the near wall and do not provide LD measurements. Besides, the mean IMT error in fully automatic methods lies in the order of 40 μm (see Table 6). The proposed method aims to automatically segment LI and MA interfaces of the far wall and the near wall interface to provide measurements of the IMT and LD in CCA ultrasound images. Our proposal segments all these interfaces and works with ultrasound images with different spatial resolutions and it was tested with three different ultrasound probes. The automatic results were compared to ground truth contours, which were calculated as the average of 4 different

manual delineations for each image. Besides, the use of frequency active contours provides soft final contours while reducing the computational cost when compared to the traditional implementation.

4.2. Manual vs. automatic IMT measurements

According to Table 4, there is a great correlation between manual and automatic IMT for all metrics, being ρ: $0.9901(PD) \cong 0.9901(MAD) > 0.9898(CLD) > 0.9471(HD)$. The error variance presents a similar trend, being around $10^{-3}mm^2$ for CLD, PD, MAD and, higher for HD ($6.6 \cdot 10^{-3}mm^2$). The correlation coefficient shows high correlation between manual and automatic IMT for all the metrics, and the mean errors present slight differences between manual and automatic measurements (see Table 4) for all metrics. Although the mean difference is lower for HD, this metric has a higher deviation, which leads to higher errors in most of the observations. This fact can be observed from Fig. 15.

Corresponding to our mostly healthy population, MAD, PD and CLD have IMT values around 0.6 mm, as can be seen from Fig. 15. Although the four metrics present high correlation with the manual measurements (see Fig. 15, Fig. 14 and Table 4), HD overestimates the IMT value when compared to the other metrics (Fig. 15). This is due to the non-linear process that calculates HD [10]. Depending on clinical criterion, HD can be an appropriate metric to measure IMT because it assures that most of the atherosclerotic patients receive treatment.

Different authors prefer the use of PD and CL [29] amongst MAD or HD, because they have into account the local orientations of the final contours to provide a more accurate IMT value. However, we should keep in mind that the manual IMT measurement is usually calculated as MAD, by both, doctors and most authors [3, 27]. Hence, to compare our method with other medical studies MAD must always be calculated. Nevertheless, PD and CLD should be considered in future studies as a standard for IMT measurement.

Considering Fig. 15, it is more common to underestimate IMT when compared to the ground truth measurements. This is due to the fact that snakes improve the segmentation process, adjusting the contours to the maximum intensity change of the edges to be found. This is the typical trend in semi or fully automated methods.

4.3. Manual vs. automatic LD measurements

The lumen diameter presents similar trends as IMT when comparing the four metrics under study (see Fig. 16 right). The error is higher than for the IMT (-65 ± 147.4 μm, when measured as MAD — see Table 4 and Fig. 16 left), but is still negligible when compared to the LD dimensions. The error between manual and automatic LD measurements is shown in Table 4 where high similarity when comparing manual and automatic LD measurements under each of the considered metrics can be appreciated.

The mean LD error is similar to other methods found in the literature (around 100 μm). For example, in [37], there are no LD error statistics, only an overlap index of 79%. In [42], the LD error is under 100 μm on average, but there is no data about statistical dispersion (see Table 6).

4.4. Distances between manual and automatic contours

Visually, automatic contours present a good agreement with manual delineation (see Fig. 13).

In Table 5 it can be seen, as a general trend, that LII interface is better detected than MAI (the mean distance with the ground truth contour is lower). For MAD, PD and CLD, LII mean distance is around 30 μm, whereas it increases to 40 μm for the MAI. Usually, LII is clearer than MAI, because the dark to bright transition is sharper than that in the MAI. This is again a common trend amongst the methods found in the literature [34]. Most referenced papers, do not present the evaluation of the similarity between manual and automatic contours; they limit to compare manual and automatic IMT measurements.

4.5. Comparison with other techniques

Table 6 shows some of the methods discussed in the Background section (4.1). Together with the main technique used, the degree of automation is displayed in the column 'Auto', which shows YES in case the method is fully-automated. In the error_{IMT} column, the mean IMT measurement error ± standard deviation is shown. Finally, the last column shows YES if the method provides LD measurements together with a LD error measure. As can be inferred from Table 6, semi-automated methods presents lower error than fully automatic proposals. This is mainly due to the fact that the user selects the region where to measure. Hence, semi-automatic methods avoid the measurement in regions where the intima-media complex cannot be seen or it is not clear.

Unlike other fully automatic methods [30, 32, 33, 34], which present an average IMT error above 20 microns, the method described here presents an error in the order of 10 microns.

The LD error is comparable to that presented by other methods or lower [42, 37] (see Table 6, in the order of 50 μm).

Amongst the automatic methods based on active contours that provide data about the execution time, running times ranging from 60 to 20s can be found. On average, our method employs 12.2 s for a single image. Besides, the segmentation provides three walls, instead of only two, like most of the automatic methods found. The images were processed on domestic performance equipment with a 2.4 GHz processor. The algorithm was implemented on a Matlab platform (R2011a).

Table 6: Some IMT measurement methods.

Author	Year	Technique	Auto	$error_{IMT}$ (μm)	LD (error μm)
Liang [20]	2000	DP	NO	42	NO
Delsanto [30]	2007	CA	YES	63±49,1	NO
Loizou [23]	2007	AC	NO	50±25	NO
Cheng [22]	2008	DP	NO	9,2±31,5	NO
Faita [31]	2008	FOAM	NO	10±35	NO
Rocha [24]	2010	DP+AC	NO	70±110	NO
Rossi [42]	2010	FOAM	YES	50± ??	YES <100
Meiburger [33]	2011	MSC	YES	39±186	NO
Molinari [34]	2011	EF	YES	43±93	NO
Xu [27]	2012	HT+AC	NO	38±16,4	NO
Petroudi [39]	2012	AC	YES	95±61,5	NO
Molinari [35]	2012	AC	YES	21±197	NO
Bastida [41]	2013	AC	YES	-	YES ?
Ilea [36]	2013	modelling	YES	80±40	NO
Loizou [37]	2013	AC	YES	30 ± 30	YES 180±150

DP: dynamic programming; AC: active contours; FOAM: First Order Absolute Moment; MSC: mean-shift classifier; EF: edge flow; HT: Hough transform;

5. Conclusions

This paper proposes a fully automated method to segment the artery walls in common carotid artery ultrasound images. Specifically, our method segments LII and MAI from far wall, as well as the NWI. With this segmentation, both, IMT and LD can be calculated along the artery length without any user interaction.

The method here presented has shown good performance with noisy and sloped images as well as images in which the carotid bulb appears. Unlike most methods, it has been tested with images taken with 3 different probes and within a spatial resolution set by the radiologist criterion (ranging from from 0.029 mm/pixel to 0.081 mm/pixel).

The solution here presented is based on a frequency implementation of active contours. Since initialization is crucial in the active contour evolution, the first step consists in locating the lumen automatically. Initialization includes speckle reduction, correlation with a model and morphological processing. After that, the Fourier domain implementation of the snakes algorithm is applied, which produces relevant computational cost savings [14]. Final contours are smooth due to the use of B-splines as shape function.

Finally, results are automatically refined by combining statistical and intensity-based strategies. This last checking step avoids the inclusion of regions which lack information in the IMT measurement. If the doctor wanted to measure at a specific point, the automatically validated results can be helpful to decide the most appropriate areas to measure IMT.

The automatic segmentation has been compared to a manual segmentation considered as ground truth, obtained as the average of four manual segmentations from two different observers. Four different metrics were assessed to measure IMT: Mean Absolute (MAD), Polyline (PD), Center Line (CLD) and Haussdorf Distance (HD). The method has been tested on a database of 46 images obtaining great correspondence with ground truth. In fact, Pearson correlation coefficient presents a range of 99 % (PD, MAD) $>$ 98.98% (CLD) $>$ 94.71% (HD) for the IMT measurement.

The mean IMT error is of 13.8 ± 31.9 μm, which is half of the IMT error for other automatic methods. For the LD, the error is comparable but lower than for other methods found. The execution time is comparable (or even lower) to other methods that do not segment the near-wall interface.

Acknowledgements

This work is supported by the Spanish Ministerio de Ciencia e Innovación, under grant TEC2009-12675, and by the Séneca Foundation (09505/FPI/08). The authors would like to thank the Radiology Department of Hospital Universitario Virgen de la Arrixaca for their kind collaboration and for providing all the ultrasound images used.

Conflict of interest

There are no conflicts of interest that could inappropriately influence this work.

[1] S. Mendis, P. Puska, B. Norrving, et al., Global atlas on cardiovascular disease prevention and control., World Health Organization, 2011.

[2] P.-J. Touboul, M. Hennerici, S. Meairs, H. Adams, P. Amarenco, N. Bornstein, L. Csiba, M. Desvarieux, S. Ebrahim, M. Fatar, et al., Mannheim carotid intima-media thickness consensus (2004–2006), Cerebrovascular diseases 23 (2007) 75–80.

[3] M. L. Bots, A. Hofman, A. M. de Bruyn, P. T. de Jong, D. E. Grobbee, Isolated systolic hypertension and vessel wall thickness of the carotid artery. the rotterdam elderly study., Arteriosclerosis, Thrombosis, and Vascular Biology 13 (1993) 64–9.

[4] M. Lorenz, H. Markus, M. Bots, M. Rosvall, M. Sitzer, Prediction of clinical cardiovascular events with carotid intima-media thickness: A systematic review and meta-analysis, Circulation: Journal of the American Heart Association 115 (2007) 459–467.

[5] K. S. Nikita, Atherosclerosis: The evolving role of vascular image analysis, Computerized Medical Imaging and Graphics (2012).

[6] J. Salonen, R. Salonen, Ultrasound b-mode imaging in observational studies of atherosclerotic progression, Circulation 87(Suppl. II) (1993) 56–65.

[7] F. Velázquez, J. D. Berná, J. L. Abellán, L. Serrano, A. Escribano, M. Canteras, Reproducibility of sonographic measurements of carotid intima-media thickness, Acta Radiologica 49 (2008) 1162–1166.

[8] J. S. Suri, R. M. Haralick, F. H. Sheehan, Greedy algorithm for error correction in automatically produced boundaries from low contrast ventriculograms, Pattern Analysis & Applications 3 (2000) 39–60.

[9] F. H. Sheehan, D. K. Stewart, H. T. Dodge, S. Mitten, E. L. Bolson, B. G. Brown, Variability in the measurement of regional left ventricular wall motion from contrast angiograms., Circulation 68 (1983) 550–9.

[10] D. Huttenlocher, G. Klanderman, W. Rucklidge, Comparing images using the hausdorff distance, Pattern Analysis and Machine Intelligence, IEEE Transactions on 15 (1993) 850 –863.

[11] R. O. Duda, P. E. Hart, Use of the hough transformation to detect lines and curves in pictures, Commun. ACM 15 (1972) 11–15.

[12] R. C. Gonzalez, R. E. Woods, S. L. Eddins, Digital image processing using MATLAB, volume 2, Gatesmark Publishing Tennessee, 2009.

[13] J. Liang, T. McInerney, D. Terzopoulos, United snakes [image analysis software], in: Computer Vision, 1999. The Proceedings of the Seventh IEEE International Conference on, volume 2, pp. 933 –940.

[14] L. Weruaga, R. Verdú, J. Morales, Frequency domain formulation of active parametric deformable models, Pattern Analysis and Machine Intelligence, IEEE Transactions on 26 (2004) 1568–1578.

[15] M. Unser, Splines: a perfect fit for medical imaging, Progress in Biomedical Optics and Imaging (2002) 225–236.

[16] L. Vincent, Morphological grayscale reconstruction in image analysis: Applications and efficient algorithms, Image Processing, IEEE Transactions on 2 (1993) 176–201.

[17] J. M. Bland, D. G. Altman, Measuring agreement in method comparison studies, Statistical methods in medical research 8 (1999) 135–160.

[18] T. Gustavsson, Q. Liang, I. Wendelhag, J. Wikstrand, A dynamic programming procedure for automated ultrasonic measurement of the carotid artery, in: Computers in Cardiology 1994, pp. 297–300.

[19] I. Wendelhag, Q. Liang, T. Gustavsson, J. Wikstrand, A new automated computerized analyzing system simplifies readings and reduces the variability in ultrasound measurement of intima-media thickness, Stroke 28 (1997) 2195–2200.

[20] Q. Liang, I. Wendelhag, J. Wikstrand, T. Gustavsson, A multiscale dynamic programming procedure for boundary detection in ultrasonic artery images, Medical Imaging, IEEE Transactions on 19 (2000) 127 –142.

[21] M. Ceccarelli, N. De Luca, A. Morganella, Automatic measurement of the intima-media thickness with active contour based image segmentation, in: Medical Measurement and Applications, 2007. MEMEA '07. IEEE International Workshop on, pp. 1–5.

[22] D.-C. Cheng, X. Jiang, Detections of arterial wall in sonographic artery images using dual dynamic programming, Information Technology in Biomedicine, IEEE Transactions on 12 (2008) 792–799.

[23] C. Loizou, C. Pattichis, M. Pantziaris, A. Nicolaides, An integrated system for the segmentation of atherosclerotic carotid plaque, Information Technology in Biomedicine, IEEE Transactions on 11 (2007) 661–667.

[24] R. Rocha, A. Campilho, J. Silva, E. Azevedo, R. Santos, Segmentation of the carotid intima-media region in b-mode ultrasound images, Image and Vision Computing 28 (2010) 614–625.

[25] F. Destrempes, J. Meunier, M.-F. Giroux, G. Soulez, G. Cloutier, Segmentation in ultrasonic B-mode images of healthy carotid arteries using mixtures of Nakagami distributions and stochastic optimization, IEEE Trans. Medical Imaging 28 (2009) 215–229.

[26] S. Golemati, J. Stoitsis, E. G. Sifakis, T. Balkizas, K. S. Nikita, Using the hough transform to segment ultrasound images of longitudinal and transverse sections of the carotid artery, Ultrasound in Medicine & Biology 33 (2007) 1918 – 1932.

[27] X. Xu, Y. Zhou, X. Cheng, E. Song, G. Li, Ultrasound intimamedia segmentation using hough transform and dual snake model, Computerized Medical Imaging and Graphics 36 (2012) 248 – 258.

[28] R. Rocha, A. Campilho, J. Silva, E. Azevedo, R. Santos, Segmentation of ultrasound images of the carotid using ransac and cubic splines, Computer methods and programs in biomedicine 101 (2011) 94–106.

[29] F. Molinari, G. Zeng, J. S. Suri, Review: A state of the art review on intima-media thickness (imt) measurement and wall segmentation techniques for carotid ultrasound, Comput. Methods Prog. Biomed. 100 (2010) 201–221.

[30] S. Delsanto, F. Molinari, P. Giustetto, W. Liboni, S. Badalamenti, J. Suri, Characterization of a completely user-independent algorithm for carotid artery segmentation in 2-d ultrasound images, Instrumentation and Measurement, IEEE Transactions on 56 (2007) 1265–1274.

[31] F. Faita, V. Gemignani, E. Bianchini, C. Giannarelli, L. Ghiadoni, M. Demi, Real-time measurement system for evaluation of the carotid intima-media thickness with a robust edge operator, Journal of Ultrasound in Medicine 27 (2008) 1353–1361.

[32] F. Molinari, W. Liboni, P. Giustetto, S. Badalamenti, J. S. Suri, Automatic computer-based tracings (act) in longitudinal 2-d ultrasound images using different scanners, Journal of Mechanics in Medicine and Biology 09 (2009) 481–505.

[33] K. M. Meiburger, F. Molinari, U. Acharya, L. Saba, P. Rodrigues, W. Liboni, A. Nicolaides, J. Suri, Automated carotid artery intima layer regional segmentation, Physics in Medicine and Biology 56 (2011) 4073–4090.

[34] F. Molinari, K. M. G. Zeng, A. Nicolaides, J. Suri, Caudles-ef: Carotid automated ultrasound double line extraction system using edge flow, Journal of Digital Imaging 24 (2011) 1059–1077.

[35] F. Molinari, K. M. Meiburger, L. Saba, G. Zeng, U. R. Acharya, M. Ledda, A. Nicolaides, J. S. Suri, Fully automated dual-snake formulation for carotid intima-media thickness measurement a new approach, Journal of Ultrasound in Medicine 31 (2012) 1123–1136.

[36] D. Ilea, C. Duffy, L. Kavanagh, A. Stanton, P. Whelan, Fully automated segmentation and tracking of the intima media thickness in ultrasound

video sequences of the common carotid artery, Ultrasonics, Ferroelectrics and Frequency Control, IEEE Transactions on 60 (2013) –.

[37] C. Loizou, T. Kasparis, C. Spyrou, M. Pantziaris, Integrated system for the complete segmentation of the common carotid artery bifurcation in ultrasound images, in: H. Papadopoulos, A. Andreou, L. Iliadis, I. Maglogiannis (Eds.), Artificial Intelligence Applications and Innovations, volume 412 of *IFIP Advances in Information and Communication Technology*, Springer Berlin Heidelberg, 2013, pp. 292–301.

[38] N. Santhiyakumari, M. Madheswaran, Extraction of intima-media layer of arteria-carotis and evaluation of its thickness using active contour approach, in: Intelligent and Advanced Systems, 2007. ICIAS 2007. International Conference on, IEEE, pp. 582–586.

[39] S. Petroudi, C. Loizou, M. Pantziaris, C. Pattichis, Segmentation of the common carotid intima-media complex in ultrasound images using active contours, Biomedical Engineering, IEEE Transactions on 59 (2012) 3060 –3069.

[40] T. F. Chan, L. A. Vese, Active contours without edges, Image Processing, IEEE Transactions on 10 (2001) 266–277.

[41] M. Bastida-Jumilla, R. Menchón-Lara, J. Morales-Sánchez, R. Verdú-Monedero, J. Larrey-Ruiz, J. Sancho-Gómez, Segmentation of the common carotid artery walls based on a frequency implementation of active contours, Journal of Digital Imaging 26 (2013) 129–139.

[42] A. Rossi, P. Brands, A. Hoeks, Automatic localization of intimal and adventitial carotid artery layers with noninvasive ultrasound: A novel algorithm providing scan quality control, Ultrasound Med Biol 36 (2010) 467–479.

[43] R.-M. Menchón-Lara, M.-C. Bastida-Jumilla, J. Morales-Sánchez, J.-L. Sancho-Gómez, Automatic detection of the intima-media thickness in ultrasound images of the common carotid artery using neural networks, Medical & biological engineering & computing 52 (2014) 169–181.